chapter
14

The Gamma Camera: Performance Characteristics

The performance of a gamma camera system is defined by the sharpness and detail of the images it produces, the efficiency with which it detects incident radiation, its ability to measure the energy of the incident γ rays (to minimize scatter), and the counting rate it can handle without significant dead time losses. A gamma camera is not capable of producing "perfect" images of the radionuclide distribution. Certain inherent imperfections arise from the performance characteristics of the detector, its associated electronic circuitry, and the collimator. Image artifacts also can be caused by malfunctions of various camera components. In this chapter, we describe the major factors that determine gamma camera performance and examine the limitations that can lead to artifacts in gamma camera images and their correction. Standard tests of gamma camera performance also are summarized.

A. BASIC PERFORMANCE CHARACTERISTICS

1. Intrinsic Spatial Resolution

Spatial resolution is a measure of the sharpness and detail of a gamma camera image. Sharp edges or small, pointed objects produce blurred rather than sharply defined images. Part of the blurring arises from collimator characteristics discussed in Sections C and D and part arises in the sodium iodide [NaI(Tl)] detector and positioning electronics. The limit of spatial resolution achievable by the detector and the electronics, ignoring additional blurring caused by the collimator, is called the *intrinsic spatial resolution* of the camera.

Intrinsic resolution is limited primarily by two factors. The first is *multiple scattering* of γ-ray photons within the detector. If a photon undergoes Compton scattering within the detector crystal and the residual scattered photon also is detected, but at some distance away, the two events are recorded as a single event occurring at a location along the line joining the two interaction sites. This is not a serious cause of degraded resolution for photon energies ≲300 keV in which multiple scatter Compton interactions in NaI(Tl) are almost negligible. Even at 662 keV, Anger calculated that for a detector thickness of 6.4 mm, less than 10% of photons are misplaced by more than 2.5 mm as a result of multiple scattering events.[1]

The second, and primary, cause of limited intrinsic resolution is statistical fluctuation in the distribution of light photons among photomultiplier (PM) tubes from one scintillation event to the next. The problem is exactly analogous to the statistical fluctuations observed in radioactive decay, discussed in Chapter 9. If a certain PM tube records, on average, N light photons from scintillation events occurring at a certain location in the detector crystal, the actual number recorded from one event to the next varies with a standard deviation given by $\sqrt{N}$. Thus if a very narrow beam of γ rays is directed at a point on the detector, the position of each event as determined by the positioning circuitry or computer algorithm is not precisely the same. Rather, they are distributed over a certain

area, the size of which depends on the magnitude of these statistical fluctuations.

A detailed method for measuring and characterizing intrinsic spatial resolution is discussed in Section E.1. Typically, a lead mask containing a number of narrow (~1 mm) slits is placed on the face of the gamma camera (without the collimator) and the camera is irradiated using a ^{99m}Tc (140-keV) point source. The resulting image is a series of lines corresponding to the locations of the slits (e.g., see Fig. 14-10A). The resolution is calculated as the full width at half maximum (FWHM) of a profile drawn perpendicular to the image of the lines at various locations in the field of view. The intrinsic spatial resolution of modern large field-of-view gamma cameras measured with ^{99m}Tc in this manner is in the range of 2.9- to 4.5-mm FWHM. Because the resolution is considerably worse than the width of the slits, the contribution of the slits themselves to the measured resolution is very small ($\leq$10% for measured resolution $\gtrsim$2.5 mm).

Intrinsic resolution becomes worse with decreasing γ-ray energy because lower-energy γ rays produce fewer light photons per scintillation event, and smaller numbers of light photons result in larger relative statistical fluctuations in their distribution (Chapter 9, Section B.1). As a rule of thumb, intrinsic resolution is proportional to $1/\sqrt{E}$, in which E is the γ-ray energy. This follows because the number of scintillation light photons produced, N, is roughly proportional to E and the relative statistical fluctuations in

their distribution are therefore proportional to $1/\sqrt{N}$. This causes noticeably greater blurring at lower γ-ray energies. An example of the change of intrinsic spatial resolution as a function of γ-ray energy is shown in Figure 14-1.

Intrinsic resolution also depends on detector crystal thickness. Thicker detectors result in greater spreading of scintillation light before it reaches the PM tubes. Furthermore, there is a greater likelihood of detecting multiple Compton-scattered events in thicker detectors, particularly with higher-energy radionuclides. These are the primary reasons why gamma cameras use relatively thin detectors in comparison with NaI(Tl) systems that are used for counting applications. Figure 14-2 shows an example of the intrinsic spatial resolution versus crystal thickness for 140-keV γ rays.

Intrinsic resolution improves with increased efficiency of collection of scintillation photons. Modern cameras are substantially improved over earlier versions in this regard because of the use of more efficient PM tubes and of better techniques for optical coupling between the detector crystal and the PM tubes. The use of greater numbers of smaller PM tubes (5-cm-diameter tubes have become the standard, and some gamma cameras have as many as 110 PM tubes per head) and improved electronics also have contributed to this improvement. Accurate corrections for nonlinearity (see Section B.1) and nonuniformity (see Section B.2) have also resulted directly in improvements in intrinsic resolution, as
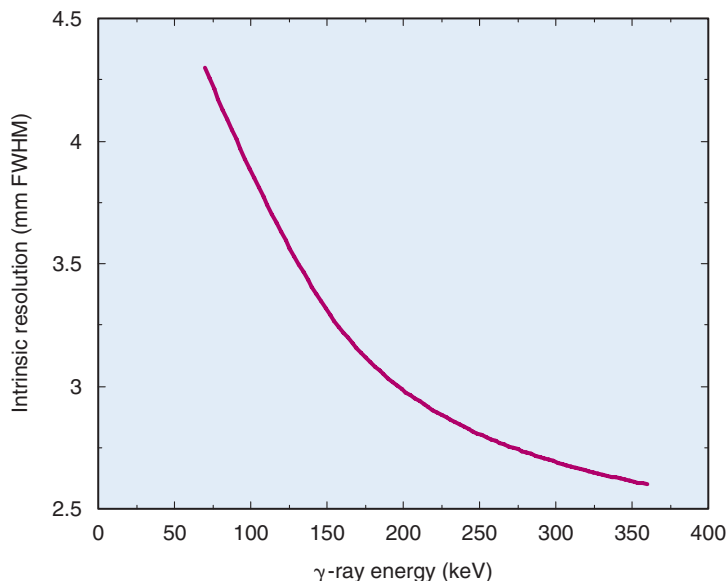

FIGURE 14-1 Intrinsic spatial resolution of a gamma camera as a function of γ-ray energy for a 6.3-mm-thick NaI(Tl) crystal. (*Compiled with data from Sano RM, Tinkel JB, LaVallee CA, Freedman GS: Consequences of crystal thickness reduction on gamma camera resolution and sensitivity.* J Nucl Med *19:712-713, 1978; and Muehllehner G: Effect of crystal thickness on scintillation camera performance.* J Nucl Med *20:992-993, 1979.*)

FIGURE 14-2 Intrinsic spatial resolution of a gamma camera at 140 keV as a function of crystal thickness. (*Compiled with data from Sano RM, Tinkel JB, LaVallee CA, Freedman GS: Consequences of crystal thickness reduction on gamma camera resolution and sensitivity.* J Nucl Med *19:712-713, 1978; Muehllehner G: Effect of crystal thickness on scintillation camera performance.* J Nucl Med *20:992-993, 1979; Royal HD, Brown PH, Claunch BC: Effects of reduction in crystal thickness on Anger camera performance.* J Nucl Med *20:977-980, 1979; Chapman D, Newcomer K, Berman D, et al: Half-inch versus quarter-inch Anger camera technology: Resolution and sensitivity differences at low photopeak energies.* J Nucl Med *20:610-611, 1979; and unpublished data from Dr. Joel Karp, University of Pennsylvania, Philadelphia, PA.*)
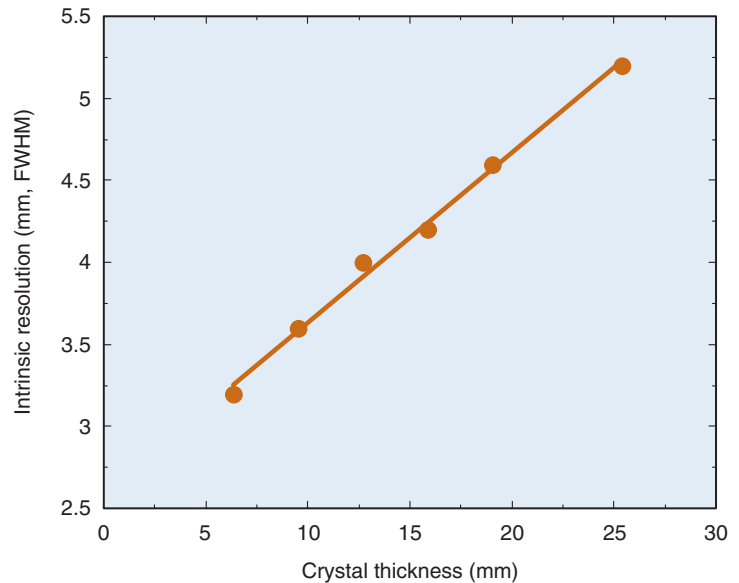
discussed in the following sections. The best reported intrinsic resolution for a large field-of-view gamma camera is just below 3 mm FWHM at 140 keV ([99mTc]). Significant improvements beyond approximately 2 mm FWHM will be difficult to achieve, owing to the ultimate limitation of the light photon yield of NaI(Tl). In most practical situations, however, the intrinsic spatial resolution makes a negligible contribution to the overall system resolution of the gamma camera, which is largely determined by the resolution of the collimator (see Sections C and D).

2. Detection Efficiency

The gamma camera employs a sodium iodide crystal that is relatively thin in comparison with most other sodium iodide detectors used in nuclear medicine: 6.4 to 12.7 mm versus 2 to 5 cm for probe counting systems, scanners, and so on. The trade-off in gamma cameras is between *detection efficiency* (which improves with thicker crystals) and intrinsic spatial resolution (which improves with thinner crystals—see Fig. 14-2). The gamma camera is designed to provide acceptable detection efficiency while maintaining high intrinsic spatial resolution in the energy range of 100-200 keV. As a result, the detection efficiency of the gamma camera detector is somewhat less than would be desirable at higher γ-ray energies.

Figure 14-3 shows photopeak detection efficiency versus γ-ray energy for the gamma camera detector for a range of NaI(Tl) crystal thicknesses. The gamma camera is nearly 100% efficient for energies up to approximately 100 keV for all crystal thicknesses, but then shows a rather marked decrease in efficiency at higher energies, depending on crystal thickness. At 140 keV (γ-ray energy of [99mTc]), the difference in efficiency between 6.4-mm and 12.7-mm-thick crystals is approximately 20% and the photopeak detection efficiency is in the 70% to 90% range. At approximately 500 keV, the standard gamma camera (detectors 0.64-0.95-cm-thick) is less than 20% efficient at converting incident γ rays into photopeak pulses.

At high energies, the performance of gamma cameras with 0.64- to 1.27-cm-thick crystals is limited by decreasing detection efficiency (as well as increasing collimator septal penetration—see Section C.2). Deteriorating intrinsic spatial resolution becomes the limiting factor at lower energies. Because of these tradeoffs, the optimal γ-ray energy range is approximately 100 to 200 keV for most gamma cameras. Some gamma cameras are now fitted with thicker crystals (12.7-25.4 mm), enabling them to achieve improved efficiency for imaging positron-emitting radionuclides at 511 keV (Chapter 18, Section B.4). This comes at the expense of some loss of intrinsic spatial resolution (see Fig. 14-2) when these systems are used in the 100-200-keV energy range.

3. Energy Resolution

It is not unusual in a typical patient study for there to be more Compton-scattered than unscattered γ rays striking the detector (see
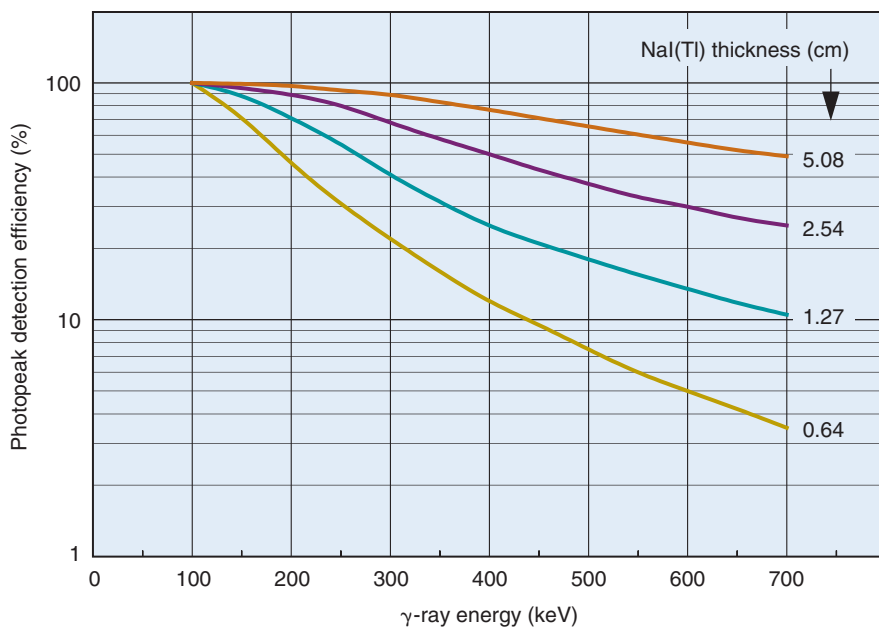
FIGURE 14-3 Photopeak detection efficiency versus γ-ray energy for NaI(Tl) detectors of different thicknesses. (*Adapted from Anger HO: Radioisotope cameras. In Hine GJ [ed]:* Instrumentation in Nuclear Medicine, *Vol 1. New York, 1967, Academic Press, p 506.*)

Fig. 11-9). Because the Compton-scattered photons have lower energy, it is possible to discriminate against them using pulse-height analysis. The energy resolution of the detector determines the efficiency with which this can be accomplished. Good energy resolution is perhaps the most important performance feature of the camera system for this purpose.

Energy resolution, like intrinsic spatial resolution, depends largely on statistical fluctuations in the number of light photons collected from a scintillation event (Chapter 10, Section B.7). Thus good light collection efficiency is a prerequisite for good energy resolution. As well, because the number of light photons released in a scintillation event increases almost linearly with γ-ray energy, E, (Fig. 10-11), energy resolution improves approximately in proportion to $1/\sqrt{E}$ (Fig. 10-13).

The energy resolution for gamma cameras is typically in the 9% to 11% range for ^{99m}Tc. Figure 14-4 shows a typical gamma camera spectrum for ^{99m}Tc with the pulse-height analyzer (PHA) window set to 130 to 150 keV. This corresponds to approximately a 15% energy window, which is a common setting for clinical studies. As illustrated by the figure, most of the events in the photopeak are accepted within this window. According to Equation 6-11, a low-energy threshold of
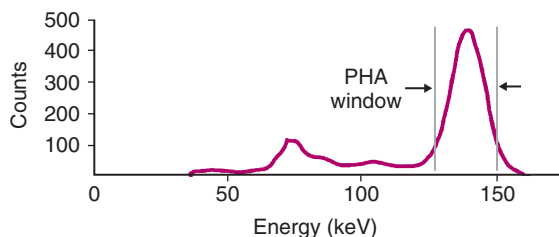

FIGURE 14-4 Energy spectrum from a gamma camera measured using a point source of ^{99m}Tc in air. The energy resolution at 140 keV in this example is 10.5%. A typical 15% energy window (approximately 130 to 150 keV) is shown superimposed on the spectrum. PHA, pulse-height analyzer. (*Data courtesy Dr. Magnus Dahlbom, UCLA School of Medicine, Los Angeles, CA.*)

130 keV should reject 140-keV γ rays that have been scattered through angles greater than approximately 45 degrees. However, because the spectrum for scattered γ rays is blurred in the same way as the spectrum for unscattered ones, the rejection efficiency for this scattering angle is only approximately 50%; half of the events produce pulses above the threshold, and half below it. This percentage would apply for 45-degree scattered 140-keV γ rays and a 130-keV lower energy level, regardless of the energy resolution of the detector. Gamma rays scattered through greater angles are rejected more efficiently,

and those scattered through smaller angles are rejected less efficiently.

Two advantages are obtained with improved energy resolution. First, the photopeak becomes narrower, resulting in more efficient detection of unscattered photons within the chosen energy window. This increases the number of valid events recorded and improves the statistical quality of the image. Second, γ rays scattered through large angles are rejected more efficiently, because their energy spread within the pulse-height spectrum is also smaller. Thus image contrast is improved. It also is true that γ rays scattered through smaller angles are detected somewhat more efficiently, because of the narrowing of their distribution as well. However, the increased efficiency for recording photopeak events more than offsets this effect, in terms of contrast-to-noise ratio (Chapter 15, Section D.2). Alternatively, one can take advantage of the improved energy resolution to use a narrower PHA window, trading back some of the increased efficiency for recording photopeak events for improved rejection of small-angle scatter. Either way, improved energy resolution results in better image quality.

4. Performance at High Counting Rates

At high counting rates, there is increased likelihood of recording two events at the same time. The most troublesome effect is known as *pulse pile-up* (Chapter 8, Section B.3). Pulse pile-up has two undesirable effects on gamma camera performance: *counting losses* and *image distortion.*

Counting losses cause inaccurate counting rates to be recorded at higher counting rates. The inaccuracies are described by conventional dead time models (Chapter 11, Section C) and may be significant in some high-count-rate quantitative studies, such as first-pass

cardiac studies. Dead time corrections can be applied; however, these corrections generally become increasingly inaccurate as counting losses increase.

Because pulse pile-up can occur between any two events in the pulse-height spectrum, system counting losses are determined by total-spectrum counting rates. Most gamma cameras behave as paralyzable systems. The apparent dead time for a selected energy window depends on the *window fraction,* that is, the fraction of the total spectrum counting rate occurring within that window. The smaller the window fraction, the larger the apparent dead time. Thus the apparent dead time is longer when a photopeak window is used than when a full-spectrum window is used. The apparent dead time also is longer when scattered radiation is present, because this also adds to the counting rate outside the photopeak window (Fig. 14-5). Therefore, when specifying gamma camera dead time, it is important to note the conditions of measurement. Dead time values as short as 1 to 2 μsec can be obtained in the absence of scattering material with a full-spectrum window; however, under clinically realistic conditions ([99mTc] source in scattering material, 15% photopeak window), system dead times of 4 to 8 μsec are more typical. For a dead time of 5 μsec, counting losses are approximately 20% for a counting rate of 4×10^4 counts per second (cps).

Dead time losses are not serious in most static imaging studies, but they can be important in certain high-counting-rate applications (e.g., first-pass cardiac studies) in which counting rates as high as 10^5 cps may occur. Pile-up rejection circuitry (see Chapter 8, Section B.3) is used to achieve higher usable counting rates in such situations. Another approach for shortening camera dead time is by the use of *analog buffers,* or *derandomizers.* These are electronic circuits that "hold" a
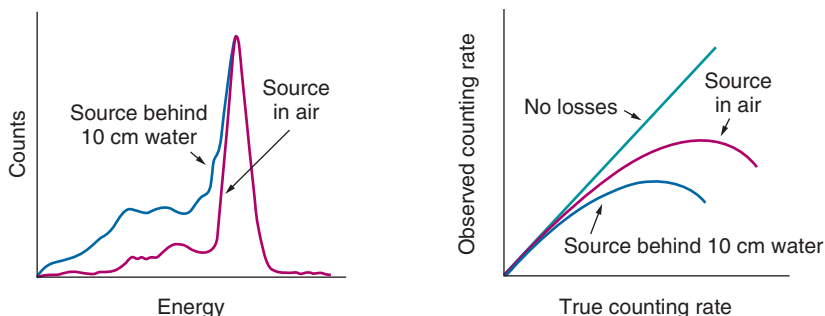

FIGURE 14-5 Effect of scattered radiation on counting losses. Scattered radiation decreases the window fraction recorded with a photopeak window (*left*), thus causing an apparent increase in dead time counting losses (*right*).

voltage level or pulse from one circuit component (e.g., an amplifier) until the next circuit in the pulse-processing sequence (e.g., the PHA) is ready to receive it.

Similarly, in digital gamma cameras, data can be buffered in memory until the computer is ready to process them. Both these approaches result in a decrease in the "apparent" dead time of the camera by effectively changing the arrival times of the pulses. This, however, means that the simple dead time models and corrections presented in Chapter 11, Section C can no longer be used, and more complex modeling of system dead time must be carried out to produce accurate correction at high counting rates.

It also is possible to physically shorten the dead time of a camera by shortening the charge integration time from the PM tubes and using electronic circuitry that returns the signal to baseline after the chosen integration time.[2] Clearly, this also decreases the amount of signal used for determining event location. For example, with a charge integration time of 0.4 μsec, only 81% of the scintillation light is collected, compared with 98% for a 1-μsec integration time. This causes a degradation of intrinsic spatial resolution and energy resolution. Some gamma cameras have a variable integration time, in which the charge integration is automatically shortened as the counting rate increases.

Other means for shortening dead time are to bypass altogether the pile-up rejection circuits and nonuniformity correction circuitry (see discussion on pile-up correction later in this section and on nonuniformity and its correction in Section B.3). The signal processing that occurs in these circuits slows down the rate at which the camera can handle individual events, and bypassing them can shorten system dead time from typical values of 4 to 8 μsec down to 1 to 3 μsec. Some cameras provide an optional "high count rate" mode of operation in which some or all of these corrections are turned off by software control. This mode is intended specifically for applications requiring high counting rates, such as first-pass cardiac studies. "Normal mode," in which all corrections are employed, is used for routine imaging to obtain the desired high-quality images. Obviously specifications for gamma camera dead time should indicate whether any circuits were bypassed to achieve the reported value.

The second undesirable effect of pulse pile-up is image distortion. Using standard pulse-positioning logic for gamma cameras

(see Chapter 13, Section B.2), two events detected simultaneously at different locations in the detector are recorded as a single event with energy equal to the sum of the two events, at a location somewhere between them (Fig. 14-6). If both are valid photopeak events, their total energy exceeds the value that would be accepted by the PHA window and both events are rejected, resulting in counting losses. On the other hand, it is possible for two Compton-scattered γ rays to have a total energy that falls within the selected energy window, so that two invalid events are accepted as a single valid event. The visible result at very high counting rates is to add a diffuse background to the image, as illustrated in Figure 14-7. Note as well the image in the upper right-hand corner of this figure, showing how contrast can be restored by shielding high-activity areas outside the imaging area of interest (e.g., with a thin sheet of lead).

Early pile-up rejection methods were based on measuring the length of a pulse. If the pulse did not return close to baseline level within the time expected given the decay time of NaI(Tl), it was assumed that pile-up of two pulses had occurred and the event was rejected, resulting in the loss of both γ rays. This improved image quality but resulted in an effective increase in system dead time, because many events were rejected at high counting rates.

Many gamma cameras now incorporate circuits that continuously monitor the decay of a pulse and use a method based on *pulse-tail extrapolation* for pile-up correction. Consider two γ-ray interactions that occur close together in time and create overlapping pulses. When the second γ ray arrives, the decay of the pulse created by the first γ ray immediately
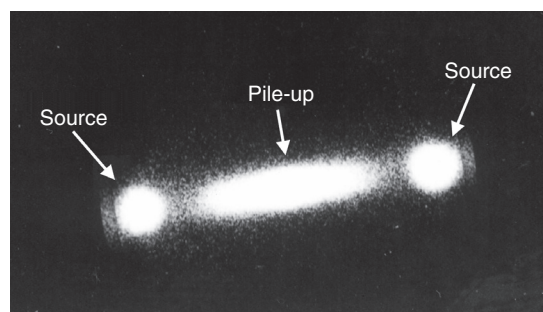

FIGURE 14-6 Images of two ⁹⁹ᵐTc point sources of relatively high activities (~370 MBq each). Events appearing in the band between the two point-source locations are mispositioned events caused by pulse pile-up.
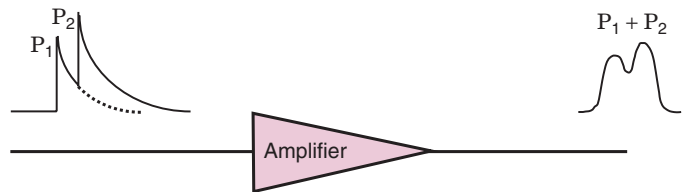
FIGURE 14-7 Demonstration of pile-up effects on images of a brain phantom. Times required to record 1.2×10^6 counts are indicated. At very high counting rates there is a noticeable loss of image contrast, which can be restored by shielding useless high-activity areas from the detector (*top right-hand image*).
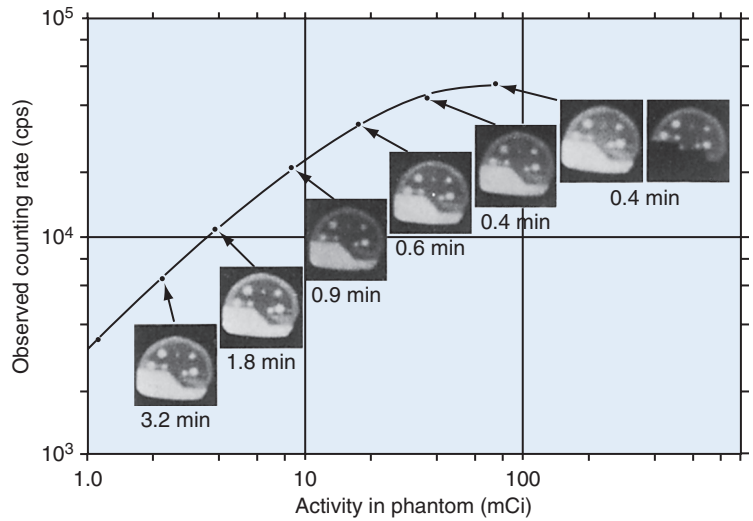
deviates from the expected exponential decay and the gamma camera signal is switched to a second amplifier circuit. Estimator circuitry in the first amplifier circuit completes the signal from the first γ ray by extrapolating the remainder of the tail of the pulse with an exponential function based on the decay time of NaI(Tl). At the same time, this extrapolated tail is also sent to the second amplifier circuit and subtracted from the second pulse. This removes the contribution of the pulse generated by the first γ ray from that of the second γ ray. This process is summarized in Figure 14-8. The pulse-tail extrapolation
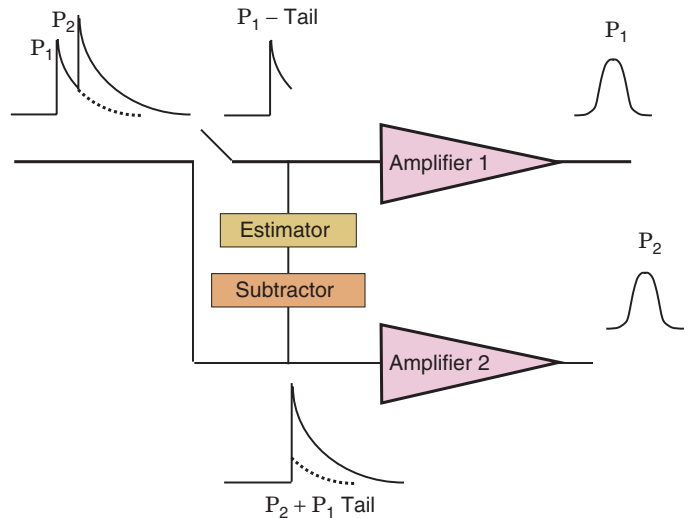

FIGURE 14-8 Illustration of pile-up correction using pulse-tail extrapolation techniques. See text for details. (*Adapted from Lewellen TK, Pollard KR, Bice AN, Zhu JB: A new clinical scintillation camera with pulse tail extrapolation electronics.* IEEE Trans Nucl Sci *37:702-706, 1990.*)

technique results in both events being retained and allows them to contribute to the image, providing they also meet the PHA requirements. This method is very effective, unless the two pulses occur nearly simultaneously (within a few tens of nanoseconds of each other), in which case the extrapolation is of limited accuracy.

With modern digital gamma cameras, it also is possible to use the spatial distribution of PM tube signals to further reduce pile-up. For pile-up events occurring at different locations in the detector crystal, two distinct clusters of PM tubes will produce signals. If the light distributions produced by the two events on the PM tubes do not overlap, or only slightly overlap, the events can be clearly separated and retained.

B. DETECTOR LIMITATIONS: NONUNIFORMITY AND NONLINEARITY

1. Image Nonlinearity

A basic problem arising in the detector and electronics is image *nonlinearity*. Straight-line objects appear as curved-line images. An inward "bowing" of line images is called *pincushion distortion;* an outward bowing is called *barrel distortion* (Fig. 14-9). Nonlinearities result when the X- and Y-position signals do not change linearly with displacement distance of a radiation source across the face of the detector. For example, when a source is moved from the edge of one of the PM tubes toward its center, the light collection efficiency of that PM tube increases more rapidly than the distance the source is moved. This causes the image of a line source crossing in front of a PM tube to be bowed toward its center. The result is a characteristic pincushion distortion in areas of a gamma camera image lying directly in front of the PM tubes, and barrel distortion between them. Differences in sensitivity among the PM tubes, nonuniformities in optical light guides, as well as PM tube or electronic malfunctions, also can cause nonlinearities.

Figure 14-10A, shows an image of a straight-line "test pattern" recorded on a
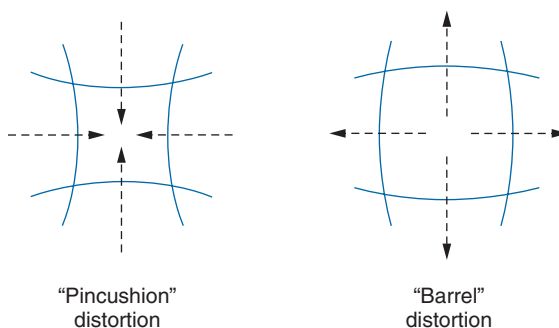
"Pincushion" distortion   "Barrel" distortion

FIGURE 14-9   Appearance of straight-line objects with "pincushion" and "barrel" distortions.

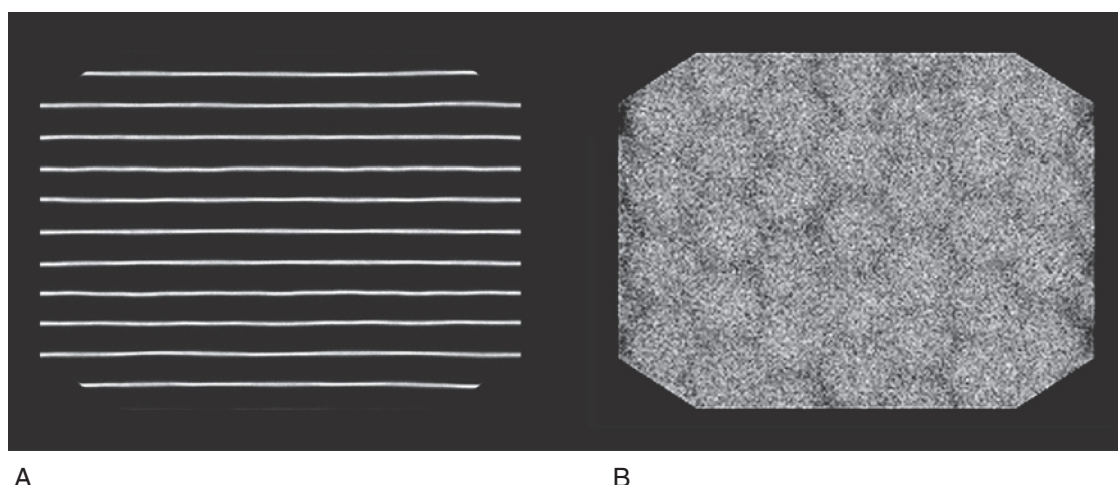A   B

FIGURE 14-10   *A,* Illustration of nonlinearities in images of a straight-line test pattern obtained with a gamma camera. Image demonstrates subtle waviness in the lines. *B,* Flood-field image obtained by exposing the same camera to a uniform radiation field. This is the image obtained in the absence of any corrections for nonuniformity. Notice that the photomultiplier tube pattern can be seen. The gray levels in this image are confined to a narrow display window to improve visualization of the artifacts. (*Images courtesy Dr. Magnus Dahlbom, UCLA School of Medicine, Los Angeles, CA.*)

modern gamma camera to demonstrate the general appearance of nonlinearities. On close inspection, some waviness of the lines is apparent. On properly functioning cameras, including the one illustrated, the nonlinearities themselves (including the pincushion distortions in front of PM tubes) are barely perceptible and rarely interfere directly with image interpretation; however, they can have significant effects on image nonuniformities, as discussed in the following section.

2. Image Nonuniformity

A more noticeable problem is image non-uniformity. Exposing the detector crystal to a uniform flux of radiation produces a *flood-field image* with small but noticeable nonuniformities in intensity, even with a properly functioning camera. These variations may be equivalent to counting rate variations of ±10% or more. A flood-field image from a gamma camera demonstrating image nonuniformity is shown in Figure 14-10B. *Intrinsic* flood-field images are acquired with the collimator removed, using a point source placed far enough from the surface of the gamma camera to give uniform irradiation of the surface (distance equal to 4-5 times the camera diameter). *Extrinsic* flood-field images are acquired with the collimator in place using a disk or thin flood phantom that covers the area of the detector. ^{99m}Tc or ^{57}Co are the two most commonly used radionuclides for flood-field measurements.

There are two primary causes of gamma camera nonuniformities. The first is *non-uniform detection efficiency* arising from (1) small differences in the pulse-height spectrum for different PM tubes and (2) position-dependent collection efficiency of scintillation light, particularly for events located over the gaps and dead areas between the PM tubes compared with events located directly over the center of a PM tube. The differences in PM tube response can be minimized by careful selection and tuning of all of the PM tubes of a gamma camera; however, position-dependent effects on the pulse-height spectrum remain. If a fixed pulse-height window is used for all output pulses, the result is an apparent difference in detection efficiency owing to differences in the "window fraction" for different areas of the crystal (see Fig. 13-6, *top*).

The second cause of nonuniformities is image *nonlinearities* described in Section B.1. In areas of pincushion distortion events are crowded toward the center of the distortion, causing an apparent "hot spot," whereas

in areas of barrel distortion events are pushed outward from the center, causing an apparent "cold spot." Because of the characteristic pincushion distortions occurring in front of PM tubes, it is common to see a pattern of hot spots at the locations of the PM tubes on an otherwise uniform gamma camera image. Other causes of nonlinearities (e.g., PM tube failure, crystal cracking, and collimator defects) also can result in nonuniformities.

Another characteristic nonuniformity is a bright ring around the edge of the image. This artifact, called *edge packing,* results from a somewhat greater light collection efficiency for events near the edge versus central regions of the detector crystal. This is the result of internal reflections of scintillation light from the sides of the detector crystal back into the PM tubes near the edge. Also, for events occurring toward the center of the crystal, there are always PM tubes on either side of the event location, whereas at the edges of the crystal there are PM tubes only to one side. Thus events at the very edges are not distributed uniformly across the edge, but are "pulled" toward the center, compounding the edge-packing artifact. The portion of the image demonstrating this artifact usually is masked on the image display and therefore is not a part of the useful field of view (UFOV). Typically, 5 cm or more of the detector width is eliminated by the mask. When specifying gamma camera detector dimensions, it is important to distinguish between the physical dimensions of the crystal and the dimensions of the useful imaging area.

Both nonuniformity and edge-packing artifacts are related to the pattern of the distribution of scintillation light falling on the PM tubes. For this reason, they also have an energy-dependent component. When the gamma camera is used to image higher-energy radionuclides, interactions, on average, occur deeper in the crystal, closer to the PM tubes. This produces a more narrow light spread distribution on the PM tubes and generally results in a worsening of detector nonuniformity.

3. Nonuniformity Correction Techniques

All modern gamma cameras incorporate techniques that attempt to correct the causes of nonuniformity described in the preceding section. All of these techniques begin with spatially varying *energy corrections,* normally derived from an intrinsic flood-field image. The flood-field image is divided into a matrix

of small, square elements, typically 128×128 elements (or *pixels*). Using the PHA, the channel number (pulse amplitude) of the photopeak in the pulse-height spectrum is determined for each element. This information is stored in a 128×128 look-up table and used to set regionally varying PHA windows for subsequent studies on patients. For example, if a 20% window is chosen for a patient study, and the center of the photopeak is found in PHA channel 100 in a particular pixel in the flood-field image, then events at that location having Z-signal amplitudes between PHA channels 90 and 110 are accepted in patient imaging studies. If the center of the photopeak is in channel 110 at another location, events for which the Z-signal falls within the range of 99 to 121 are accepted at that location. The position-dependent PHA window corrects for variations in the pulse-height spectrum across the face of the camera detector. It also provides a partial correction for image nonuniformity.

The second step in the nonuniformity correction is to account for the remaining regional variations in image intensity, largely caused by detector nonlinearity. In one older method, the correction is based directly on variations in intensity of the energy-corrected flood-field image. The number of counts recorded within each pixel in that image is stored in a matrix and compared to the smallest number recorded in the pixel array. This is used to derive a matrix of normalized intensity values, which range from 100 for the "coldest" pixel to higher values for other pixels. In subsequent patient studies, a certain fraction of the

counts recorded in each pixel are thrown out, depending on the relative value for that pixel in the energy-corrected flood-field image. For example, if the value in the normalized intensity-correction matrix is 110, then 1 of every 11 counts is subtracted from the patient image at that location. This process is sometimes called *count skimming*.

Most modern digital gamma cameras replace the second step described in the preceding paragraph with a correction for image nonlinearity, which more directly attacks the major underlying cause of image nonuniformity. For nonlinearity corrections, another flood-field image is obtained, this time with a sheet of lead having a uniformly spaced array of small holes (~1-mm diameter, ~4-mm separation) placed directly on the gamma camera face (no collimator). The locations of the images of these holes are compared with their known locations in the lead sheet to derive a matrix of offsets, Δx and Δy, for each (X, Y) location on the detectors, which is stored as another look-up table. When an event is detected, its X and Y coordinates are computed using conventional positional circuitry or algorithms. These values then are corrected using the positional offsets for that location stored in the look-up table. The offsets and the corresponding look-up table usually are measured and generated at the factory prior to shipment.

Figure 14-11 shows the same data as Figure 14-10, after the corrections for nonuniformity and nonlinearity described in the preceding paragraphs have been applied. Figure 14-12, showing intensity profiles across the flood-field images in Figures 14-10 and 14-11,
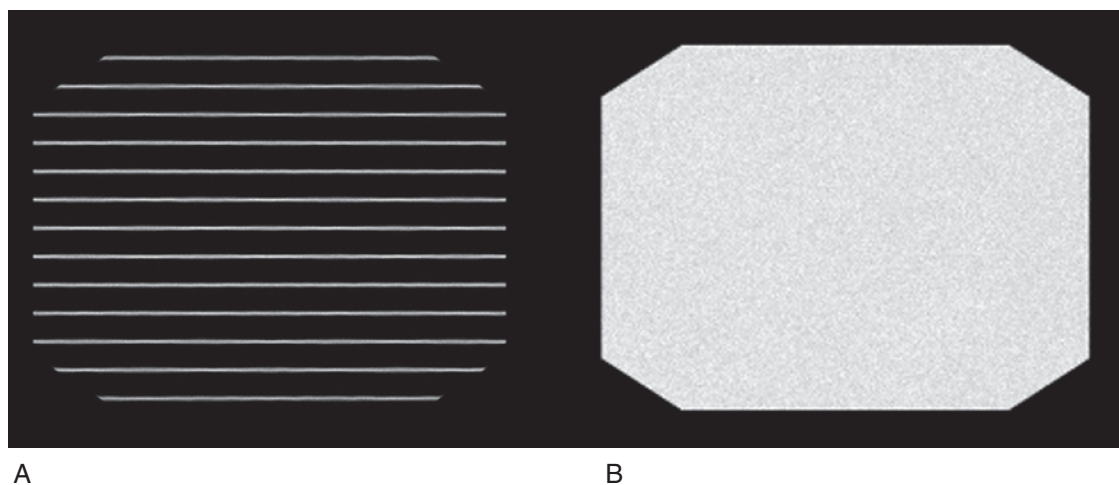

FIGURE 14-11 Straight-line test pattern (*A*) and uniform flood-field (*B*) images after nonuniformity corrections are applied. Compare with Figure 14-10. (*Images courtesy Dr. Magnus Dahlbom, UCLA School of Medicine, Los Angeles, CA.*)
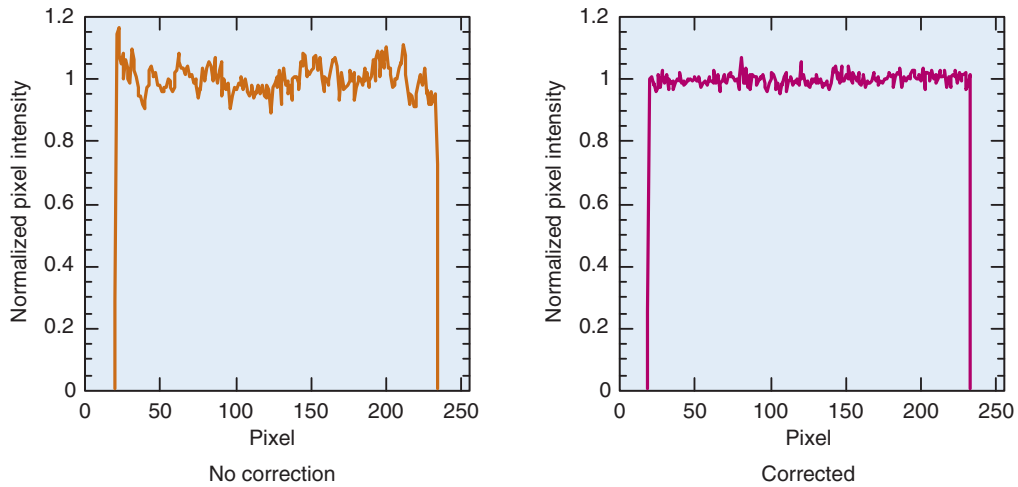
FIGURE 14-12   Profiles through the uniform flood-field images in Figures 14-10 and 14-11 showing relative uniformity of flood-field image with and without nonuniformity correction. The standard deviation is improved from 3.4% to 1.9% after correction.

clearly illustrates the improvements. The examples in these figures are for ^{99m}Tc. Note that different correction matrices must be obtained for each radionuclide used, because the effects corrected for generally vary with γ-ray energy, for example, because of different average depths of interaction in the NaI(Tl) crystal.

Improvements in camera uniformity also have contributed to improvements in intrinsic resolution. Earlier cameras used thicker light guides and large-diameter PM tubes, in part to achieve satisfactory uniformity, at the expense of somewhat degraded spatial resolution. Because of effective uniformity corrections, newer gamma cameras can use thinner light guides (or eliminate the light guide entirely) and smaller PM tubes, both of which contribute to more accurate event localization and improved intrinsic spatial resolution.

4. Gamma Camera Tuning

The nonuniformity corrections described previously require that the gamma camera remain very stable over time. However, the gain of PM tubes invariably changes as the tubes age. The high-voltage supply and amplifier gain can also drift over time. A method to "tune" the PM tubes to ensure consistent performance over time is therefore necessary.

On many older systems, the tuning is done manually. One method involves irradiation of the gamma camera detector through a lead mask with holes centered over each of the PM tubes. The output of each PM tube is examined and the preamplifier gain is adjusted if the tube output has changed by more than 1% from the original reference value.

In newer gamma cameras, the large number of PM tubes makes the manual method impractical. Many digital gamma cameras therefore contain tuning circuitry that allows the output of each individual PM tube to be automatically adjusted to a set of reference outputs. One automated approach involves the use of light-emitting diodes (LEDs) that are coupled to the neck of each PM tube. These LEDs are pulsed to produce a light signal on the photocathode of the PM tube that does not vary with time. The PM tube signals are then monitored and the preamplifier adjusted electronically if the PM tube signal has drifted.

A second approach uses two narrow energy windows, placed just above the photopeak position to minimize the influence of scatter (Fig. 14-13). The count ratio between the two energy windows during flood-field irradiation by the radionuclide of interest is measured for each PM tube. This ratio remains constant, unless the PM tube signal drifts over time. If the count ratio changes, the PM tube preamplifier is adjusted electronically to restore the ratio to its original value.

Some of these tuning methods also can be adapted so that they are continuous, in the sense that the camera is tuned dynamically every few seconds during a patient study. This can be used to adjust the energy windows in real time, compensating for any drift that occurs during the course of a study. The major cause of drift on such short
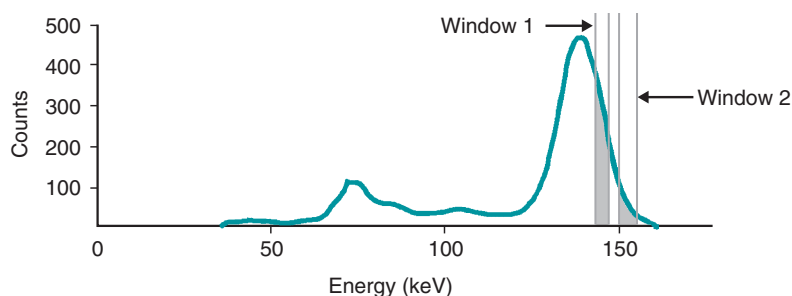
FIGURE 14-13 The ratio of counts detected in two narrow energy windows can be used to determine whether a photomultiplier tube is drifting. The windows are defined on the high side of the photopeak to avoid any contribution from scatter. The ratio is virtually independent of source distribution and the amount of scattering material present.

timescales usually is related to count-rate effects. At high counting rates, a small baseline shift can occur in the signal amplitudes owing to overlap of pulses, and continuous adjustment of the energy window minimizes such effects, keeping the energy window centered over the photopeak irrespective of the counting rate. Continuous tuning also is important in single photon emission computed tomographic imaging (Chapter 17), in which rotation of the gamma camera through the earth's magnetic field can result in changes of PM tube gain. A detailed discussion of automatic tuning methods can be found in reference 3.

C. DESIGN AND PERFORMANCE CHARACTERISTICS OF PARALLEL-HOLE COLLIMATORS

1. Basic Limitations in Collimator Performance

The collimator is a "weak link" for the performance of a gamma camera system, as indeed it is in any nuclear medicine imaging system employing the principles of *absorptive collimation. Collimator efficiency,* defined as the fraction of γ rays striking the collimator that actually pass through it to project the γ-ray image onto the detector, is typically only a few percent or less. *Collimator resolution,* which refers to the sharpness or detail of the γ-ray image projected onto the detector, also is rather poor, generally worse than the intrinsic resolution of the camera detector and electronics.

Because it is a limiting factor in camera system performance, it is important that the collimator be designed carefully. Poor design can result only in poorer overall performance. Design considerations for parallel-hole collimators are discussed in this section. Design characteristics for converging and diverging collimators are similar to those of the parallel-hole type. Design characteristics of pinhole collimators are not discussed in detail here but are described in references 4 and 5. The analysis to be presented for parallel-hole collimators is similar to that presented by Anger in reference 1, which may be consulted for a more detailed discussion.

2. Septal Thickness

A primary consideration in collimator design is to ensure that *septal penetration* by γ rays crossing from one collimator hole into another is negligibly small. This is essential if an accurate γ-ray image is to be projected by the collimator onto the camera detector. No thickness of septal material is sufficient to stop *all* γ rays, so the usual criteria is to accept some reasonably small level of septal penetration (e.g., ~5%).

The required septal thickness can be determined by analysis of Figure 14-14. The shortest path length for γ rays to travel from one hole to the next is w. Septal thickness t is related to w, and to the length l and diameter d of the collimator holes, by

$$t \approx 2dw/(l-w) \qquad (14\text{-}1)$$

If septal penetration is to be less than 5%, the transmission factor for the thickness w must be

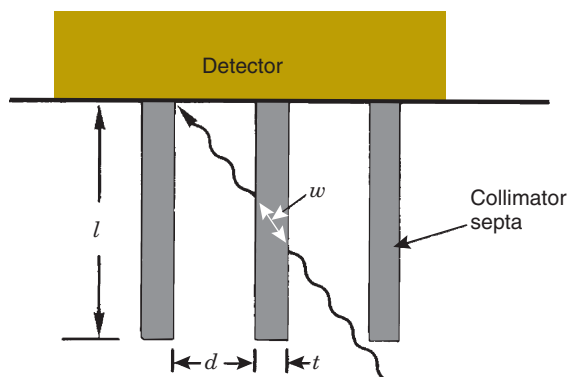$$e^{-\mu w} \lesssim 0.05 \qquad (14\text{-}2)$$

FIGURE 14-14 Minimum path length w for a γ ray passing through the collimator septa from one hole to the next depends on length l and diameter d of the collimator holes and on septal thicknesses t.

where μ is the linear attenuation coefficient of the septal material. Because e^{-3} is approximately 0.05, this implies

$$\mu w \gtrsim 3 \qquad (14\text{-}3)$$

$$w \gtrsim 3/\mu \qquad (14\text{-}4)$$

and thus

$$t \gtrsim \frac{6d/\mu}{l-(3/\mu)} \qquad (14\text{-}5)$$

It is desirable that septal thickness t be as small as possible so that the collimator septa obstruct the smallest possible area of detector surface and collimator efficiency is maximized. This objective is realized by using a material with a large value of μ for the collimator septa. Materials of high atomic number Z and high density ρ are preferred. Lead (Z = 82, ρ = 11.3 g/cm³) is the material of choice for reasons of cost and availability; however, other materials, including tantalum (Z = 73, ρ = 16.6 g/cm³), tungsten (Z = 74, ρ = 19.3 g/cm³), gold (Z = 79, ρ = 19.3 g/cm³) and even depleted uranium (Z = 92, ρ = 18.9 g/cm³) have been employed in experimental applications.

As discussed in Chapter 6, Section D.1, attenuation coefficients of heavy elements depend strongly on γ-ray energy in the nuclear medicine energy range. Thus the required septal thickness also depends strongly on the γ-ray energy for which the collimator is designed to be used. Commercially available collimators are categorized according to the maximum γ-ray energy for which their septal thickness is considered to be adequate. *Low-energy collimators* generally have an upper limit of approximately 150 keV and *medium-energy collimators* of approximately 400 keV. *High-energy collimators* are used for imaging positron-emitting radionuclides at 511 keV.

EXAMPLE 14-1

Calculate the septal thickness required for low-energy (150 keV) and medium-energy (400 keV) lead collimators having hole diameters of 0.25 cm and lengths of 2.5 cm.

Answer
The linear attenuation coefficient of lead at 150 keV is μ_l = 1.91 cm²/g × 11.34 g/cm³ = 21.66 cm⁻¹ and at 400 keV is μ_l = 0.22 cm²/g × 11.34 g/cm³ = 2.49 cm⁻¹ (Appendix D). Therefore from Equation 14-5 for the low-energy collimator

$$t \gtrsim \frac{6 \times 0.25/21.66}{2.5-(3/21.66)}$$

$$\gtrsim 0.029 \text{ cm}$$

and for the medium-energy collimator

$$t \gtrsim \frac{6 \times 0.25/2.49}{2.5-(3/2.49)}$$

$$\gtrsim 0.465 \text{ cm}$$

As shown by this example, thicknesses needed for low-energy collimators are only a few tenths of a millimeter, which is in the range of lead "foil" thicknesses and approaches the limits of lead thicknesses that can be used without loss of necessary mechanical strength. Indeed, low-energy collimators generally are quite fragile, and their septa can be damaged easily by mechanical abuse (such as dropping or stacking on sharp objects). Medium-energy collimators require substantially greater septal thicknesses, typically a few millimeters of lead. Alternatively, medium-energy collimators can be made thicker (larger l in Equation 14-5).

Low-energy γ-ray emitters (e.g., ⁹⁹ᵐTc, 140 keV) can be imaged using medium-energy collimators. This is done, however, with an unnecessary sacrifice of collimator efficiency because the collimator septa are unnecessarily thick. (See Table 14-1 for comparative efficiencies of low- and medium-energy collimators.) Low-energy collimators are used whenever possible to obtain maximum collimator efficiency. When choosing a collimator, however, one must consider not only the energy of the γ rays to be imaged but also the energies of any other γ rays emitted by the radionuclide of

interest or by other radionuclides that may be present as well (e.g., residual activity from another study or radionuclide impurities). Higher-energy γ rays may be recorded by Compton downscatter into a lower-energy analyzer window. If the collimator septa are too thin, the collimator may be virtually transparent to higher-energy γ rays, causing a relatively intense "foggy" background image to be superimposed on the desired image, with a resulting loss of image contrast. Whether a low-energy collimator can be used when higher-energy γ rays are present depends on the energy and intensity of those emissions and requires experimental evaluation in specific cases.

3. Geometry of Collimator Holes

Collimator performance also is affected by the geometry of the collimator holes, specifically, their *shape, length,* and *diameter*. The preferred hole shape, to maximize the exposed area of detector surface for a given septal thickness, is round or hexagonal, with the holes arranged in a close-packed hexagonal array, or square holes in a square array. Triangular holes also have been used.

Collimator hole length and diameter affect strongly both collimator resolution and collimator efficiency. Collimator resolution R_{coll} is defined as the FWHM of the radiation profile from a point or line source of radiation projected by the collimator onto the detector (Fig. 14-15). This profile is also called the *point-spread function* (PSF) or *line-spread function* (LSF). Collimator resolution R_{coll} is given by*

$$R_{coll} \approx d(l_{eff} + b)/l_{eff} \qquad (14\text{-}6)$$

where b is the distance from the radiation source to the collimator and d is the diameter and $l_{eff} = l - 2\mu^{-1}$ the "effective length" of the collimator holes. Here μ is the linear attenuation coefficient of the collimator material. The effective length of the collimator holes is somewhat less than their actual length owing
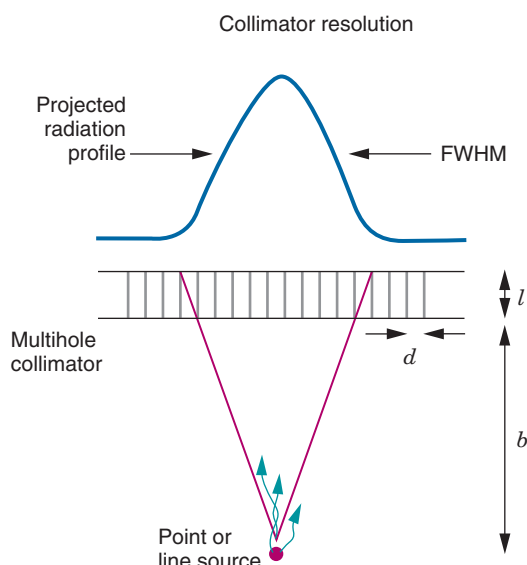
---

*Some versions of Equation 14-6 include additional correction terms involving the thickness of the detector crystal, reflecting the fact that the image actually is formed at some depth within the detector crystal. Because photons of different energies penetrate to different average depths within the crystal, the correction actually is photon-energy dependent, a point not noted in some texts. The correction is small and for simplicity is omitted from Equation 14-6, as well as from Equations 14-10 and 14-13 for the converging and diverging collimators presented later in this chapter.

FIGURE 14-15 Radiation profile (point- or line-spread function) for a parallel-hole collimator. The full width at half maximum (FWHM) of the profile is used to characterize collimator resolution.

to septal penetration. For 2.5-cm thick low-energy collimators (150 keV), the difference between effective and actual length is approximately 0.1 cm, whereas for 2.5-cm thick medium-energy collimators (400 keV) it is approximately 0.8 cm.

EXAMPLE 14-2

Calculate the resolution (FWHM) of the low-energy collimator described in Example 14-1, at source depths $b = 0$ and $b = 10$ cm, assuming it has a septal thickness of 0.03 cm.

Answer
The effective length of the collimator is

$$l_{eff} = 2.5 \text{ cm} - (2/21.66) \text{ cm} \approx 2.4 \text{ cm}$$

Thus for $b = 0$

$$R_{coll} \approx 0.25 (2.4 + 0)/2.4 \text{ cm}$$
$$\approx 0.25 \text{ cm}$$

and at $b = 10$ cm

$$R_{coll} \approx 0.25 (2.4 + 10)/2.4 \text{ cm}$$
$$\approx 1.3 \text{ cm}$$

This example illustrates the strong dependence of collimator resolution on the distance of the source from the collimator.

Collimator efficiency g, defined as the fraction of γ rays passing through the collimator per γ ray emitted by the source is given by

$$g \approx K^2 (d/l_{\mathrm{eff}})^2 [d^2/(d+t)^2] \qquad (14\text{-}7)$$

where t is septal thickness and K is a constant that depends on hole shape (~0.24 for round holes in a hexagonal array, ~0.26 for hexagonal holes in a hexagonal array, ~0.28 for square holes in a square array[1]). Equation 14-7 applies to a source *in air* and assumes no attenuation of radiation by intervening body tissues.

Several aspects of Equations 14-6 and 14-7 should be noted. First, resolution improves as the ratio of hole diameter to effective length (d/l_{eff}) is made smaller. Long, narrow holes provide images with the best resolution; however, collimator efficiency decreases approximately as the square of the ratio of hole diameter to length $(d/l_{\mathrm{eff}})^2$. Thus an approximate relationship between collimator efficiency, g, and spatial resolution, R_{coll}, is

$$g \propto (R_{\mathrm{coll}})^2 \qquad (14\text{-}8)$$

Therefore for a given septal thickness, collimator resolution is improved only at the expense of decreased collimator efficiency, and vice versa.

EXAMPLE 14-3

Calculate the efficiency g of the collimator described in Examples 14-1 and 14-2, assuming it has hexagonal holes in a hexagonal array.

Answer
For hexagonal holes in a hexagonal array, $K = 0.26$. Thus,

$g \approx (0.26)^2 (0.25/2.4)^2 \times [(0.25)^2/(0.25+0.03)^2]$

$\approx (0.0676) \times (0.0109) \times (0.797)$

$\approx 5.85 \times 10^{-4}$
(photons transmitted/photons emitted)

This example illustrates the relatively small fraction of emitted γ rays that are transmitted by a typical gamma camera collimator.

Equation 14-7 also demonstrates the effect of septal thickness on efficiency. Medium-energy collimators have lower efficiencies than low-energy collimators because of their greater septal thicknesses.

In addition to providing low- and medium-energy collimators, manufacturers of gamma camera systems also provide a selection of collimators with different combinations of resolution and efficiency. Those with good resolution but poor efficiency generally are described as "high-resolution" collimators, whereas those with the opposite characteristics are described as "high-sensitivity" collimators. Those with characteristics intermediate to the extremes are referred to as "general purpose," "all purpose," or by other similar names.

Equation 14-6 indicates that collimator resolution becomes poorer as source-to-collimator distance b increases. Thus structures closest to the collimator are imaged with sharpest detail. Figure 14-16 shows graphically the relationship between collimator resolution and source-to-collimator distance for three different collimators provided by one commercial manufacturer. Typically, collimator resolution deteriorates by a factor of 2 at a distance of 4-6 cm from the collimator.

On the other hand, according to Equation 14-7, collimator efficiency for a source in air is independent of source-to-collimator distance b. This rather surprising result is obtained provided the counting rate for the entire detector area is measured. The reason for this is illustrated by Figure 14-17. As the source is moved farther away from the collimator, the efficiency with which radiation is transmitted through any one collimator hole decreases in proportion to $1/b^2$ (inverse-square law), but the number of holes through which radiation can pass to reach the detector increases in proportion to b^2. The two effects cancel each other, with the result that total counting rate—and thus collimator efficiency—does not change with source-to-collimator distance. Another illustration of this effect is shown in Figure 14-18. As source-to-collimator distance increases, the maximum height of the PSF or LSF decreases, but the width increases (and resolution becomes poorer), so that the total area under the curve (total detector counting rate) does not change.

Invariance of collimator efficiency with source-to-collimator distance applies to point sources, line sources, and uniform sheet sources in air with parallel-hole collimators; however, it applies only to uniform sheet sources with converging, diverging, or pinhole collimators (Section D). When the source is embedded at different depths in the patient, attenuation effects also must be considered. Septal penetration and scatter of photons from the walls of the collimator holes also are not considered in the earlier analysis.
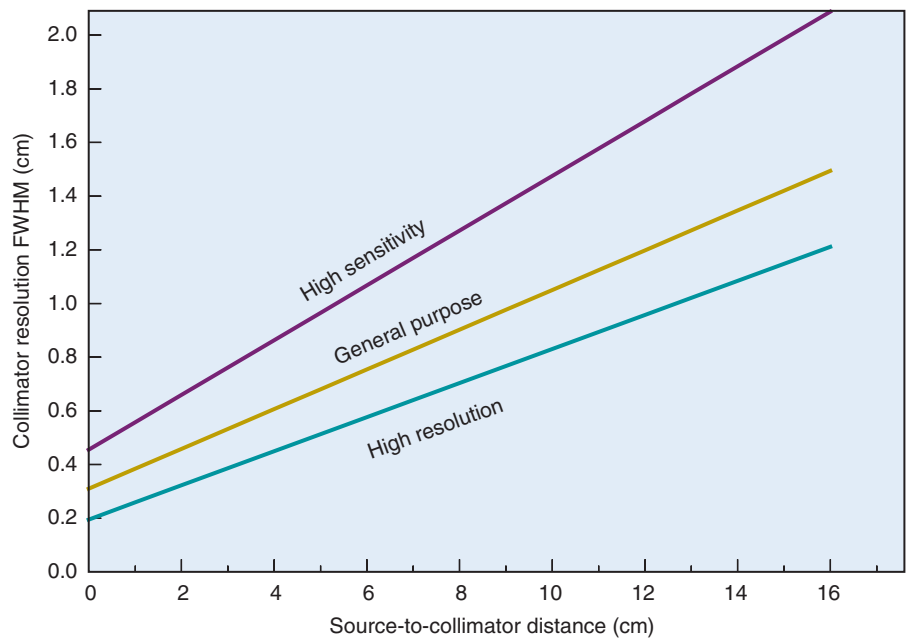
FIGURE 14-16 Collimator resolution versus source-to-collimator distance for three different collimators. (*Adapted from Hine GJ, Paras D, Warr CP: Recent advances in gamma-camera imaging.* Proc SPIE *152:123, 1978.*)
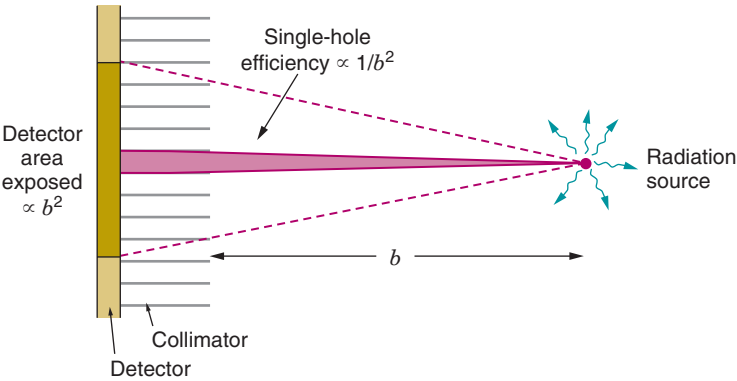

FIGURE 14-17 Explanation for constant counting rate (collimator efficiency) versus source-to-collimator distance for a point source in air and a parallel-hole collimator. Efficiency for a single hole decreases as $1/b^2$, but number of holes passing radiation (area of detector exposed) increases as b^2.
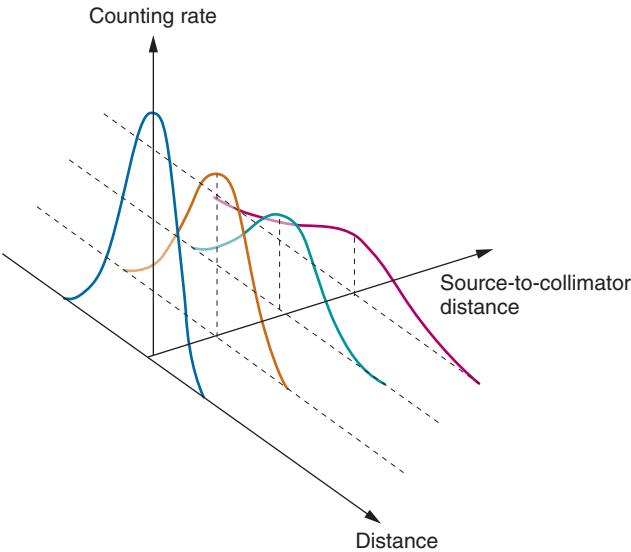

FIGURE 14-18 Point-spread functions versus distance for a parallel-hole collimator. Area under curve is proportional to collimator efficiency and does not change with distance.

PERFORMANCE CHARACTERISTICS OF SOME TYPICAL COMMERCIALLY MANUFACTURED PARALLEL-HOLE COLLIMATORS

Collimator Type	Recommended Max. Energy (keV)	Efficiency, g	Resolution R_{coll} (FWHM at 10 cm)
Low-energy, high-resolution	150	1.84×10^{-4}	7.4 mm
Low-energy, general-purpose	150	2.68×10^{-4}	9.1 mm
Low-energy, high-sensitivity	150	5.74×10^{-4}	13.2 mm
Medium-energy, high-sensitivity	400	1.72×10^{-4}	13.4 mm

Adapted from Hine GJ, Erickson JJ: Advances in scintigraphic instruments. In Hine GJ, Sorenson JA (eds): *Instrumentation in Nuclear Medicine*, Vol 2. New York, 1974, Academic Press.

FWHM, full width at half maximum.

Table 14-1 summarizes the physical construction and typical performance characteristics of a number of collimators. Collimator resolution is the FWHM for a source at 10 cm from the face of the collimator. Collimator efficiency g refers to the relative number of γ rays transmitted by the collimator and reaching the detector per γ ray emitted by the source. Note that the approximate relationship between collimator efficiency and resolution given by Equation 14-8 is verified by these data. Note also the relatively small values for collimator efficiency.

4. System Resolution

The sharpness of images recorded with a gamma camera is limited by several factors, including intrinsic resolution, collimator resolution, scattered radiation, and septal penetration. In terms of the FWHM of a PSF or LSF, the most important factors are the intrinsic resolution R_{int} of the detector and electronics, and the collimator resolution R_{coll}. The combined effect of these two factors is to produce a *system resolution R_{sys}* that is somewhat worse than either one alone. System resolution R_{sys} (FWHM) is given by

$$R_{sys} = \sqrt{R_{int}^2 + R_{coll}^2} \qquad (14\text{-}9)$$

Because collimator resolution depends on source-to-collimator distance, system resolution also depends on this parameter. Figure 14-19 shows system resolution versus source-to-collimator distance for a typical parallel-hole collimator and different values of intrinsic resolution. At a distance of 5-10 cm (typical depth of organs inside the body), *system resolution* is much poorer than intrinsic resolution and is determined primarily by *collimator resolution*. There are significant differences between system resolutions for cameras having substantially different intrinsic resolutions (e.g., 4 mm vs. 8 mm), but the difference in system resolutions for cameras having small differences in intrinsic resolutions (e.g., 4 mm vs. 5 mm) is minor and not clinically significant. Small differences in intrinsic resolution may be apparent on bar-pattern images or on images of very superficial structures in the patient, but they usually are not apparent on images of deeper-lying structures.

System resolution also is degraded by scattered radiation. This is discussed in Chapter 15, Section C. The method for combining component resolutions to determine system resolution also is discussed in Appendix G.

D. PERFORMANCE CHARACTERISTICS OF CONVERGING, DIVERGING, AND PINHOLE COLLIMATORS

Figure 14-20 illustrates the important design parameters for converging, diverging, and pinhole collimators. Equations for collimator resolution, R_{coll}, and efficiency, g, for these collimators are as follows:

Converging Collimator:

$$R_{coll} \approx [d(l'_{eff} + b)/l'_{eff}][1/\cos\theta] \\ \times [1 - (l'_{eff}/2)/(f + l'_{eff})] \qquad (14\text{-}10)$$

$$g \approx K^2(d/l'_{eff})^2[d^2/(d+t)^2][f^2/(f-b)^2] \qquad (14\text{-}11)$$

where

$$l'_{eff} \approx (l - 2\mu^{-1})/\cos\theta \approx l_{eff}/\cos\theta \qquad (14\text{-}12)$$
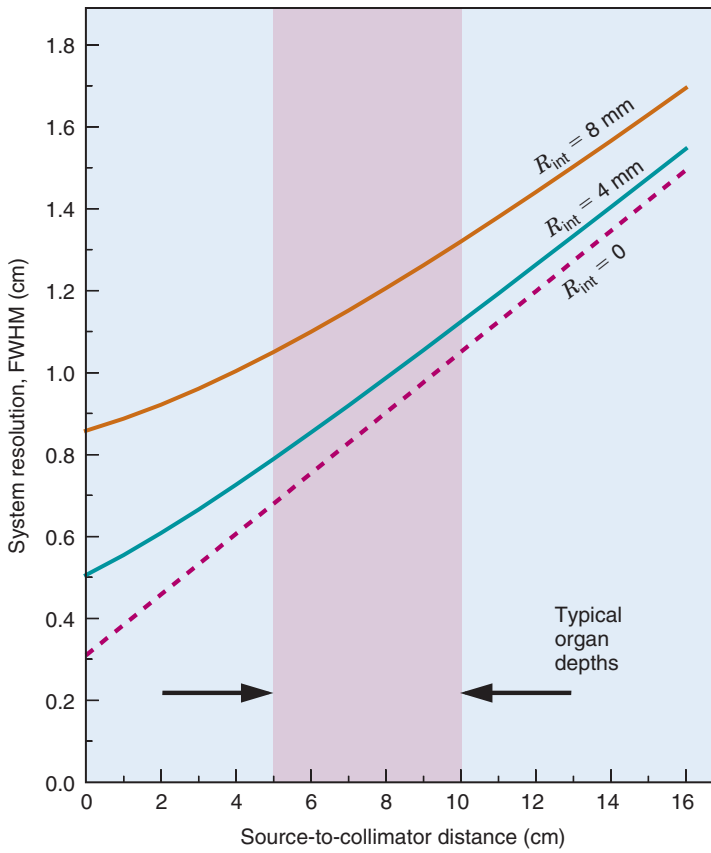
FIGURE 14-19 System resolution versus source-to-collimator distance for a typical parallel-hole collimator and different values of intrinsic resolution. At most typical organ depths, system resolution is determined primarily by collimator resolution.
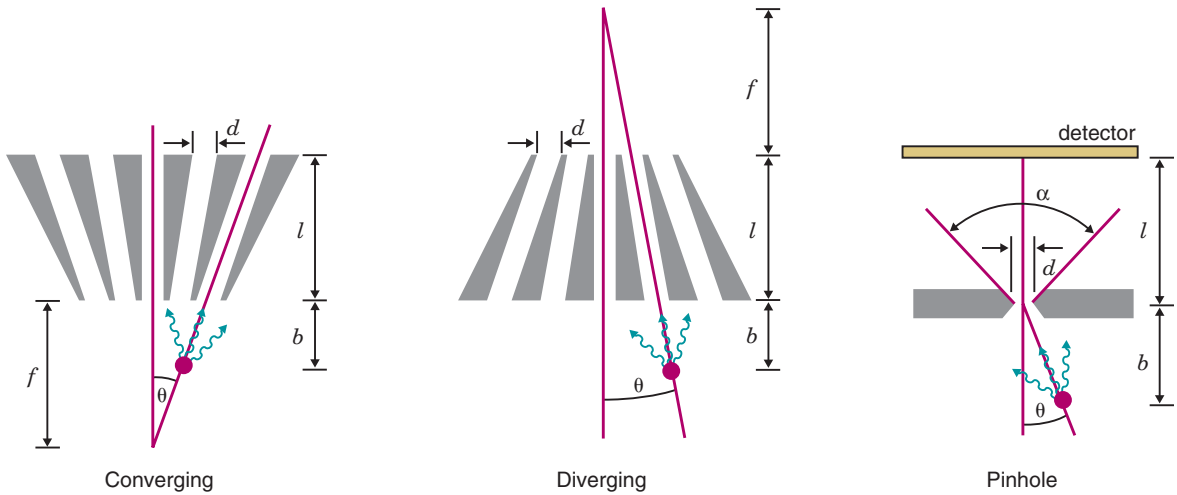
FIGURE 14-20 Parameters for collimator resolution R_{coll}, and efficiency, g, for Equations 14-10 to 14-18.

Diverging Collimator:

$$R_{\mathrm{coll}} \approx [d(l'_{\mathrm{eff}} + b)/l'_{\mathrm{eff}}][1/\cos\theta][1 + (l'_{\mathrm{eff}}/2f)] \tag{14-13}$$

$$g \approx K^2(d/l'_{\mathrm{eff}})^2[d^2/(d+t)^2][(f+l)/(f+l+b)] \tag{14-14}$$

Pinhole Collimator:

$$R_{\mathrm{coll}} \approx d_{\mathrm{eff,R}}(l+b)/l \tag{14-15}$$

$$g \approx d_{\mathrm{eff,g}}{}^2 \cos^3\theta/(16b^2) \tag{14-16}$$

where

$$d_{\text{eff,R}} = d + \frac{\ln(2)}{\mu}\tan\left(\frac{\alpha}{2}\right) \quad (14\text{-}17)$$

and

$$d_{\text{eff,g}} = \sqrt{d[d + (2/\mu)\tan(\alpha/2)] + [(2/\mu^2)\tan^2(\alpha/2)]} \quad (14\text{-}18)$$

l'_{eff} is the effective collimator length, accounting for septal penetration at different off-axis locations (see also Equation 14-6). For the pinhole collimator, $d_{\text{eff,R}}$ and $d_{\text{eff,g}}$ are the "effective" pinhole diameters, for resolution and sensitivity, respectively. d_{eff} takes into account the penetration of gamma rays through the edges of the pinhole aperture, but still assumes parallel rays, normally incident on the detector surface.[4,5] These expressions for d_{eff} also assume that the pinhole aperture has a "knife-edge" geometry, as illustrated in Figure 14-20.

The equations for collimator resolution R_{coll} refer to the equivalent FWHM of the PSF or LSF, corrected for magnification or minification of the image by the collimator described by Equations 13-3, 13-5, and 13-6. Thus, if the collimator projects a profile with a 2-cm FWHM measured on the detector and the image magnification factor is ×2, the equivalent FWHM in the imaged plane is 1 cm.

These equations may be compared with Equations 14-6 and 14-7 for the parallel-hole collimator. They are similar except for the presence of additional terms involving collimator focal lengths f and, for off-axis sources, the angle θ between the source, the focal point (or pinhole), and the central axis of the collimator. The equations illustrate that for converging and diverging collimators, resolution is best at the center (θ = 0, cos θ = 1).

The performance characteristics of different types of collimators are compared in Figure 14-21, which shows *system* resolution and efficiency versus distance, including effects of camera intrinsic resolution as well as collimator magnification. Equations 14-10, 14-13, and 14-15 show that resolution *always* is best with the source as close as possible to the collimator. Changes in collimator efficiency with distance depend on whether the radiation source is a point source or a uniform sheet source.

For a point source (Fig. 14-21, *right*), collimator efficiency increases with increasing source-to-collimator distance for the converging collimator. Maximum efficiency is obtained at the collimator convergence point

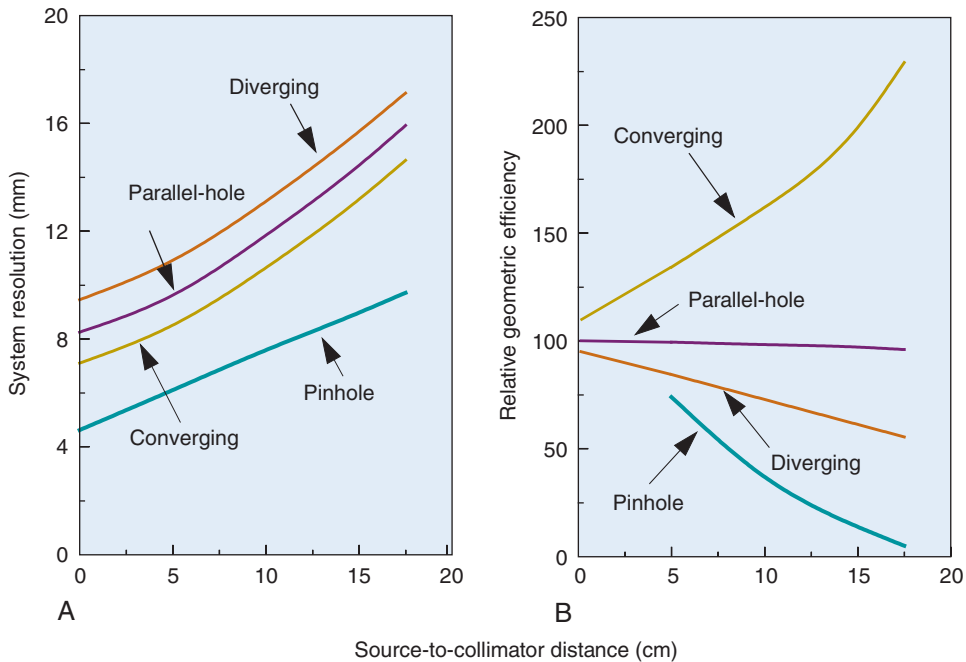

FIGURE 14-21   Performance characteristics (*A,* system resolution; *B,* point-source geometric efficiency in air) versus source-to-collimator distance for four different types of gamma camera collimators. (*Adapted with permission from Society of Nuclear Medicine from Moyer RA: A low-energy multihole converging collimator compared with a pinhole collimator.* J Nucl Med *15:59-64, 1974.*)

(~35 cm), where γ rays are transmitted through all of the collimator holes, and then decreases beyond that point. Point-source collimator efficiency decreases with distance for the diverging and pinhole collimators, more severely for the latter. For an extended, large-area sheet source, sufficiently large to cover the entire field of view of the collimator, efficiency does not change with source-to-collimator distance for all of these collimators. Again, for sources embedded within a patient, attenuation effects also must be accounted for.

Figure 14-21 illustrates that the converging collimator offers the best combination of resolution and efficiency at typical imaging distances (5 to 10 cm); however, the field-of-view is also somewhat limited at these distances (Equation 13-6 and Example 13-2), and for this reason converging collimators are most useful with cameras having relatively large-area detectors. Diverging collimators offer a larger imaging area (Example 13-1) but at the cost of both resolution and efficiency. Pinhole collimators offer very good resolution and reasonable efficiency at close distances but lose efficiency very rapidly with

distance; they also have a quite limited field of view because of magnification effects at typical imaging distances (Equation 13-3). Generally they are used for imaging smaller organs, such as the thyroid and heart, which can be positioned close to the collimator. They also are useful with high-energy γ-ray emitters because they can be designed to reduce septal penetration problems.

Differences between the resolution and field-of-view obtained at different source-to-collimator distances with parallel-hole, converging, diverging, and pinhole collimators are further illustrated by Figure 14-22. The distortions caused by changing magnification with depth for different structures inside the body sometimes make images obtained with the converging, diverging, and pinhole collimators difficult to interpret (see Fig. 13-9).

E. MEASUREMENTS OF GAMMA CAMERA PERFORMANCE

It is important to define standardized experimental protocols for measuring gamma camera performance that produce consistent

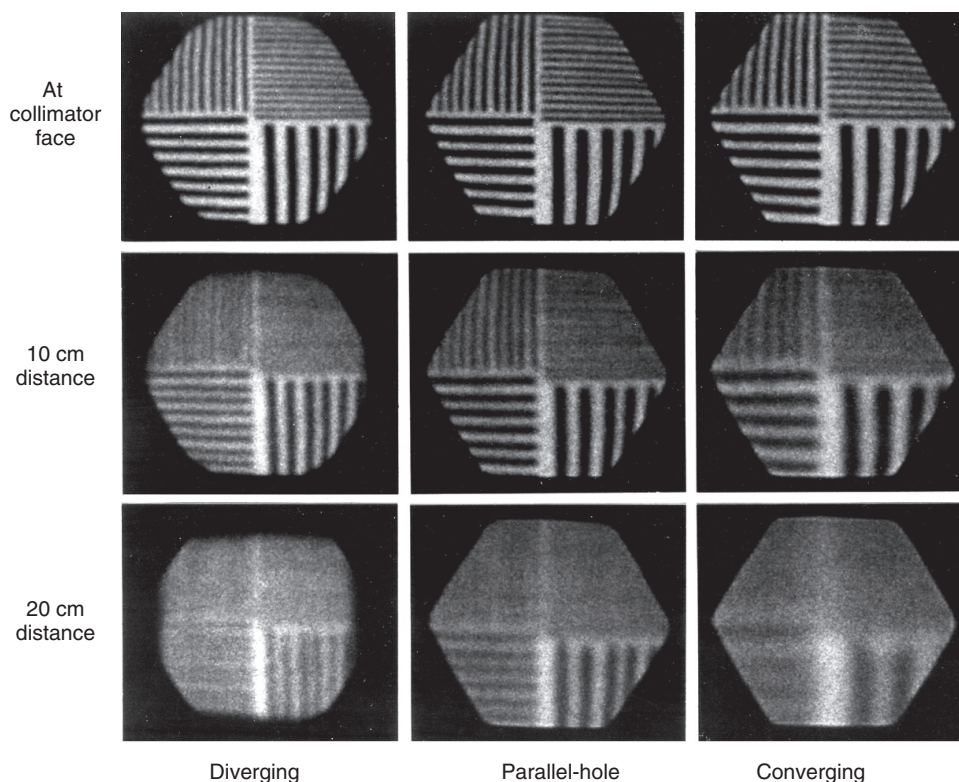| At collimator face | | |
10 cm distance		
20 cm distance		
Diverging	Parallel-hole	Converging

FIGURE 14-22 Bar-pattern images demonstrating changing field size and resolution obtained versus distance for three collimator types.

results, are easily reproducible, and that do not require specialized equipment. Such protocols can then be used in comparing one gamma camera with another, in performing acceptance testing on a newly installed gamma camera, and as part of a quality assurance program to ensure that the camera is always performing to its specifications.

The exact regulations for gamma camera quality assurance and the guidelines for acceptance testing vary with locality. For example, in the United States, the Joint Commission requires that instruments be tested prior to initial use and that the performance of a gamma camera be tested at least once a year. Because of the rapidly changing regulatory environment, and differences between states and countries, a detailed review of the requirements of regulatory agencies is beyond the scope of this book. In this section, we therefore briefly summarize the more common measurements that are performed to assess gamma camera performance (whether they be for acceptance testing or for quality assurance). The protocols presented here are largely based on the recommendations of the National Electrical Manufacturers Association.[6] A typical quality assurance program might involve daily measures of flood-field uniformity, weekly checks of spatial resolution and spatial linearity, and semiannual checks of other performance parameters. It is important that all measurements be taken under the same conditions (pulse-height window width, correction algorithms, and correction circuitry on or off) as are used for routine clinical studies. More detailed information on performance measurements, quality assurance, and acceptance testing can be found in references 7 to 9.

1. Intrinsic Resolution

Intrinsic resolution is determined without a collimator using a linearity test pattern, such as the one shown in Figure 14-10 (*left*), placed directly on the surface of the NaI(Tl) crystal housing. The width of the strips in the pattern is approximately 1 mm, which is significantly smaller than the resolution expected in the measurement. A point source (usually ^{99m}Tc or ^{57}Co) is placed at a distance equal to five times the UFOV from the gamma camera face. The UFOV corresponds to the field of view of the gamma camera after masking off the portion of the camera face affected by edge-packing effects. Data are acquired with the system count rate below 30,000 cps

(<10,000 cps for a small field-of-view gamma camera) to avoid pile-up-related mispositioning. Two sets of images are taken, with a 90-degree rotation of the test pattern between acquisitions so that both X and Y resolution are measured. Data are acquired until the peak channel has at least 1000 counts. Images are acquired in a matrix with pixel sizes less than $\frac{1}{10}$ of the expected resolution (typically <0.35 mm). Profiles through the images of the line sources are taken at different locations across the gamma camera face and fitted to a Gaussian function (Chapter 9, Section B.3). The FWHM (Fig. 14-15) and full width at tenth maximum (FWTM) of the profiles are measured in both X and Y directions. The reported measurements usually are average measurements across the UFOV, and the average across the central field-of-view (CFOV) that has linear dimensions scaled by 75% with respect to the dimensions of the UFOV. Typical values of intrinsic spatial resolution are 2.5 to 3.5 mm.

2. System Resolution

This measurement is made with the collimator in place and should be repeated for each collimator of interest. The source consists of two 1-mm-diameter line sources, placed 5 cm apart at a distance of 10 cm from the front face of the collimator. The measurement also can be performed with the addition of a scattering medium by placing 10 cm of plastic between the sources and the collimator, and 5 cm of the same material behind the sources. Images are acquired (typically several million events, at a rate of <30,000 cps to avoid pileup) and profiles taken through the image of the line sources are fitted to Gaussian functions to determine FWHM and FWTM as described for intrinsic resolution. The results vary widely depending on the exact type of collimator used but are typically in the range of 8 to 14 mm for ^{99m}Tc.

3. Spatial Linearity

This measurement uses the same slit pattern (Fig. 14-10A) and conditions as for the intrinsic resolution measurement. Once again, measurements are taken with two orientations of the test pattern, rotated by 90 degrees, to provide linearity measurements in both X and Y directions. Two measurements can be made from the resulting images. The *differential spatial linearity* is the deviation of the measured distance d_i between two slits from the actual distance D between them calculated for each row i in the image. The means

and the standard deviations are reported for the X and Y directions across the UFOV and the CFOV and are defined as:

$$\text{Mean} = \frac{\sum_{i=1}^{n}(d_i - D)}{n} \qquad (14\text{-}19)$$

$$\text{Standard Deviation} = \sqrt{\frac{\sum_{i=1}^{n}(d_i - D)^2}{n-1}} \qquad (14\text{-}20)$$

In addition, the *absolute spatial linearity* is defined as the maximum deviation of the location of the slits from their true location. Once again this is assessed for the UFOV and the CFOV. It is not easy to detect small nonlinearities using these techniques, and tests of uniformity (discussed in the next section) usually are better at revealing the effects of small nonlinearities.

4. Uniformity

Intrinsic uniformity is determined from flood-field images acquired without a collimator. A ^{99m}Tc source is placed at a distance of approximately $5 \times$ the UFOV from the front face of the gamma camera. The source activity is such that the counting rate on the gamma camera is less than approximately 30,000 cps. Flood-field images are acquired so that there are a minimum of 4000 counts in each pixel of the image and then smoothed with a 9-point (3×3) smoothing filter with the following weightings:

$$
\begin{array}{ccc}
1 & 2 & 1 \\
2 & 4 & 2 \\
1 & 2 & 1
\end{array}
$$

Integral uniformity is based on the maximum and minimum pixel counts in the image and is defined as

Integral Uniformity (%)

$$= 100 \times \frac{\text{max. pixel count} - \text{min. pixel count}}{\text{max. pixel count} + \text{min. pixel count}} \qquad (14\text{-}21)$$

This is calculated for the UFOV and CFOV. Integral uniformity values are typically 2% to 4%.

Differential uniformity is based on the change in counts of five consecutive pixels across all rows and columns of the image. It is defined as

$$\text{Differential Uniformity (\%)} = 100 \times \frac{(\text{high} - \text{low})}{(\text{high} + \text{low})} \qquad (14\text{-}22)$$

where "high" refers to the maximum count difference for any five consecutive pixels (row or column) in the image and "low" refers to the minimum count different for any five consecutive pixels. This usually is reported for the UFOV.

For convenience, uniformity measurements often are made with the collimator in place (*extrinsic uniformity*). A thin flood-field source of ^{99m}Tc or a disk source of ^{57}Co that covers the active area of the gamma camera is placed on top of the collimator to provide uniform irradiation. This protocol is more practical for routine quality assurance because the measurement can be done without removing the collimator. Extrinsic uniformity measurements also have the advantage that they reveal any defects or problems caused by the collimator itself.

5. Counting Rate Performance

As described in Section A.4, most gamma cameras behave as paralyzable counting systems with the observed count rate described as a function of the true count rate by Equation 11-18. The basis for measurement of the dead time, τ, is the two-source method described in Chapter 11, Section C.4. Two ^{99m}Tc sources are placed approximately 1.5 m away from the camera face. The total activity should be sufficient to cause approximately a 20% loss in the observed counting rate relative to the true counting rate. Counting rates then are measured with both sources present, and then with each individual source present. Care must be taken that all measurements are performed with exactly the same source geometry, that pile-up rejection electronics or any other high counting rate correction circuitry is turned on, and that source decay is negligible (<1%) during the course of the measurement. The dead time can then be calculated from Equation 11-25. The observed count rate at which a 20% counting rate loss occurs, $R_{20\%}$, is also often quoted, and this can be computed from Equation 11-18 using the fact that $R_o = 0.8R_t$ as

$$R_{20\%} = -\frac{0.8}{\tau}\ln(0.8) \qquad (14\text{-}23)$$

6. Energy Resolution

Energy resolution is measured with a flood illumination of the gamma camera face, without a collimator, using a ^{99m}Tc source suspended $5 \times$ UFOV above the camera face. The resulting pulse-height spectrum is analyzed to determine the FWHM of the ^{99m}Tc photopeak. It usually is reported in keV or converted to a percent energy resolution based on the energy of the photopeak (see Equation 10-3). Typical values are in the range of 8% to 11% for ^{99m}Tc.

7. System Sensitivity

System sensitivity needs to be measured separately for each collimator. In general, the sensitivity of low-energy collimators is measured with ^{99m}Tc ($E_\gamma = 140$ keV), that of medium-energy collimators is measured with ^{111}In ($E_\gamma = 172$, 247 keV), and ^{131}I ($E_\gamma = 364$ keV) is used for high-energy collimators. A solution of the radionuclide (known total activity) is placed in a 10-cm diameter dish to a depth of 2 to 3 mm. The shallow depth minimizes self-absorption by the source. The source is placed 10 cm from the front face of the collimator and an image is acquired. The sensitivity is calculated by drawing a circular region of interest around the image of the dish and integrating all the counts in that region. A second image is recorded for an equal imaging time with the source removed to provide a measure of the background. The same region of interest is applied to this image. The sensitivity is given by

$\text{Sensitivity(cps/Bq)}$

$$= \frac{\text{counts in ROI} - \text{background counts in ROI}}{\text{time(sec)} \times \text{source activity(Bq)}}$$

$$(14\text{-}24)$$

A general-purpose collimator typically has a sensitivity on the order of 2 to 3×10^{-4} cps/Bq or 0.02% to 0.03%.

REFERENCES

1. Anger HO: Radioisotope cameras. In Hine GJ, editor: *Instrumentation in Nuclear Medicine*, Vol 1. New York, 1967, Academic Press, pp 485-552.
2. Muehllehner G, Karp JS: A positron camera using position-sensitive detectors: PENN-PET. *J Nucl Med* 27:90-98, 1986.
3. Graham LS: Automatic tuning of scintillation cameras: A review. *J Nucl Med Tech* 14:105-110, 1986.
4. Accorsi R, Metzler SD: Analytic determination of the resolution-equivalent effective diameter of a pinhole collimator. *IEEE Trans Med Imag* 23:750-763, 2004.
5. Smith MF, Jaszczak RJ: The effect of gamma ray penetration on angle-dependent sensitivity for pinhole collimation in nuclear medicine. *Med Phys* 24:1701-1709, 1997.
6. Performance measurements of scintillation cameras. Standards Publication No. NU-1-2007. Washington, DC, 2007, National Electrical Manufacturers Association.
7. Simmons GH, editor: *The Scintillation Camera*, New York, 1988, Society of Nuclear Medicine.
8. Graham LS: Scintillation camera imaging performance and quality control. In Henkin RE, Boles MA, Karesh SM, et al, editors: *Nuclear Medicine*, St. Louis, 1996, Mosby, pp 125-146.
9. Murphy PH: Acceptance testing and quality control of gamma cameras, including SPECT. *J Nucl Med* 28:1221-1227, 1987.